WILEY-VCH

DOI: 10.1002/ ((please add manuscript number))
Article type: Full paper

Characterization of Basic Physical Properties of Sb_2Se_3 and its relevance for photovoltaics

*Chao Chen, Ye Yang, David C. Bobela, Shuaicheng Lu, Kai Zeng, Bo Yang, Liang Gao, Matthew C. Beard, Jiang Tang**

C. Chen, S. Lu, K. Zeng, B. Yang, L. Gao, Prof. J. Tang
Wuhan National Laboratory for Optoelectronics (WNLO), Huazhong University of Science and Technology, 1037 Luoyu Road, Wuhan, 430074, Hubei, China.
Email: jtang@mail.hust.edu.cn

Dr. Y. Yang, Dr. D. C. Bobela and Dr. M. C. Beard
Chemistry and Nanoscience Center, National Renewable Energy Laboratory, Golden, CO, 80401

Keywords: Sb_2Se_3, mobility, lifetime, diffusion length, defects

Sb_2Se_3 is an efficient absorption layer in solar cells because of its attractive material, optical and electric properties. In recent years, the power conversion efficiency of Sb_2Se_3 thin film solar cells has gradually enhanced to 5.6%. In this article, we systematically researched the basic physical properties of Sb_2Se_3 such as dielectric constant, anisotropic mobility, carrier lifetime, diffusion length, defect depth, defect density and optical band tail states. We believe such a comprehensive characterization of the basic physical properties of Sb_2Se_3 lays a solid foundation for further optimization of solar device performance.

1. Introduction

Antimony selenide (Sb_2Se_3), a semiconductor possessing one dimensional crystal structure,[1] is an excellent photovoltaic absorber due to its high absorption coefficient (>10^5 cm^{-1}) at visible region;[2] 1.17 eV band gap (optimal for single junction solar

cells),[3] simple binary composition with fixed orthorhombic phase,[4] low toxicity, and earth-abundant constituents. What's more, theoretical calculation and experimental characterizations confirmed that Sb_2Se_3 has benign grain boundaries (GBs) if properly aligned along the c-direction.[5] In recent years, through steady improvements in the growth of these aligned $Sb2Se_3$ films,power conversion efficiency (PCE) of Sb_2Se_3 thin film solar cells has increased to 5.6%,[5-6] which is larger than other non-cubic semiconductor thin film solar cells such as SnS thin film solar cells (reported best PCE of 4.6%).[7]

Despite the rapid improvement, the device efficiency is still far behind conventional copper indium gallium selenide (CIGS, PCE=22.3%),[8] cadmium telluride (CdTe, PCE=22.1%)[9] , copper zinc tin sulfoselenide (CZTSSe, PCE=12.6%)[10], and even amorphous silicon (PCE=XXX, look up in PIPV tables) solar cells. One reason is that the fundamental features of thin film Sb_2Se_3 such as mobility, carrier lifetime, diffusion length, defect depth, defect density and band tail remain largely unexplored. Only film conductivity and carrier mobilities were reported in few previous studies.[11] The study on Sb_2Se_3 is lacking because of three difficulties: the intrinsically low electrical conductivity (10^{-6}-10^{-7} Scm^{-1}) of Sb_2Se_3 film creates obstacles forobtaining carrier density and mobility directly from Hall effect measurement; the absence of photoluminescence due to its indirect bandgap makes iobtaining carrier lifetime and defect information challenging; and the strong anisotropy in Sb_2Se_3 crystal renders mobility measurements very complicated. Nevertheless, understanding these fundamental parameters of thin film Sb_2Se_3 is of

great importance to device configuration design, performance, and optimization. Given the great potential already demonstrated, further investigation of these properties is urgently needed.

In this letter, time of fight (TOF) measurement were used to determine the anisotropic mobilities. Time-resolved transient absorption (TA) spectroscopy was used to probe dynamics of photogenerated carriers, and thus determine carrier lifetimes. [12] Electron diffusion length was directly characterized through biased internal quantum efficiency (IQE) measurement, and was calculated from the mobility-lifetime product as well. Temperature dependent dark conductivity and thermal admittance spectroscopy (TAS) was applied to determine the depth and density of defect states in thin film Sb_2Se_3 , respectively. Lastly, photothermal deflection spectroscopy (PDS) was used to probe disorder by measuring optical band tails of crystal Sb_2Se_3 (c-Sb_2Se_3) and amorphous Sb_2Se_3 (a-Sb_2Se_3) films. A table summarizing all the parameters is included for readers' convenience, followed by the discussion of their relevance for photovoltaic application. We believe such a comprehensive characterization of the basic physical properties of Sb_2Se_3 film lays a solid foundation for further optimization of device performance.

2. Results and Discussion

2.1 Dielectric constant as a function of frequency

We have to emphasize that all the experimental characterizations presented in this paper were carried out on Sb_2Se_3 films produced by rapid thermal evaporation (RTE) because RTE so far produced the best photovoltaic device. [5] The only

exception was the cylindrical Sb_2Se_3 for dielectric constant measurement which was fabricated by hot-pressed process. Please take caution when apply the results obtained here to Sb_2Se_3 film produced by other methods since film morphology, orientation and defects could vary which would significantly influence film mobility, carrier lifetime, defect distribution and so on.

Since dielectric constant is relevant to many physical properties, we first tested the dielectric constant in the frequency range of 2 kHz to 2 MHz with an Agilent E4980A using the parallel plate capacitor configuration. The device structure is Au/Sb_2Se_3/Au with the hot-pressed cylindrical Sb_2Se_3 (diameter=13 mm, thickness=1 mm) sandwiched between two YY thick Au electrodes (as the inset in **Figure** 1). The dielectric constant related to the capacitance via::

$$C=\frac{\varepsilon_r \varepsilon_0 A}{d} \quad (1)$$

where ε_r is the dielectric constant, ε_0 is the vacuum permittivity, A is the area of electrodes, d is the thickness of Sb_2Se_3. As shown in Figure 1, the dielectric constant is larger than 29 at low frequency (~2 kHz) and stays approximately constant at 18 at radio-wave frequencies (~2 MHz), which is close to its optical dielectric constant of 14.3 (~10^{14} Hz).[3] This value is higher than copper indium diselenide (CIS, 15.2) and CdTe (10.0) in which the exciton binding energy was estimated to be 4.5 and 10.5 meV, respectively.[13] We thus believe that excitons immediately dissociate into free electrons and holes upon generation in Sb_2Se_3 films, unlike in polymer absorbers where the low dielectric constant leads to strong exciton binding, which consequently necessitates the a bulk heterojunction architecture for efficient exciton dissociation.[14]

Free electrons and holes being the preponderant carriers in the operating device also implies their field assisted transport and compliance with the established working principles of thin film solar cells.

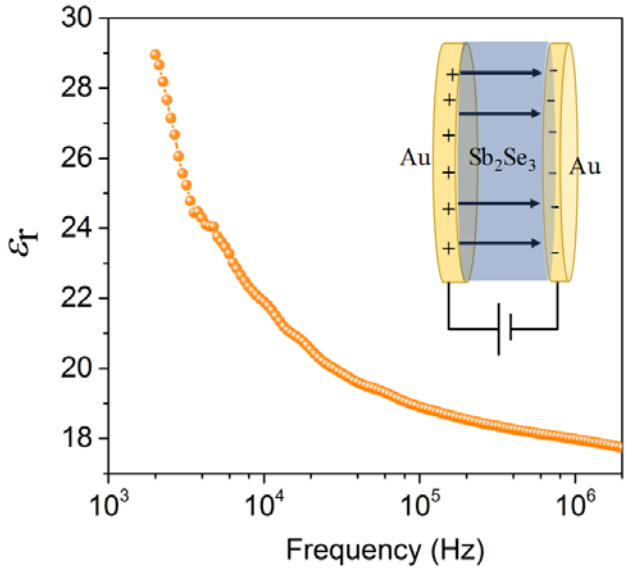

Figure 1. The frequency dependent dielectric constant of Sb_2Se_3. The inset is the ilustration of the parallel plate capacitor with the interspcaing between Au electrodes as 1 mm.

2.2 Mobility

Mobility of the absorber material is an important parameter to be considered when designing and optimizing the device configuration. Sb_2Se_3 crystal is composed of one dimensional $(Sb_4Se_6)_n$ ribbons with orthorhombic crystal structure and a space group of Pnma 62.[5] It has strong covalent bonds along the [001] axis while only weak van der Waals bonds present in the [100] and [010] axis. For simplicity, we call direction along [100], [010] and [001] axis as a-, b- and c-direction, respectively. Low crystal symmetry would render high mobility anisotropy in Sb_2Se_3, which can be measured by the TOF method [reference]. TOF measurement need to meet the following conditions: (1) a transparent electrode allowing light illumination from at

least one side, (2) pulsed excitation light with energy much larger than the material's band gap so that the absorption depth is much smaller than the sample thickness. We intentionally produce thick films to ensure film thickness is much larger than absorption depth. (3) RC time constant, the product of the circuit resistance (in ohms) and the circuit capacitance (in farads), much smaller than the transit time. Our device structure for TOF measurement was ITO/Sb_2Se_3/Au. A pulse laser with the wavelength of 532 nm was incident from ITO and a large number of electron-hole pairs were produced in the Sb_2Se_3 region close to ITO because of the large absorption coefficient (>10^5 cm^{-1}) of Sb_2Se_3 for 532 nm photons. Electrons were quickly extracted by ITO, while holes driven by the applied bias have to travel through the thick Sb_2Se_3 films. The hole mobility could be extracted by the Equation (2):[15]

$$\mu=\frac{d^2}{V\tau_t} \quad (2)$$

where μ is mobility, d is film thickness, V is the driving voltage and τ_t is the transit time.

To measure the anisotropic mobility, three different orientated Sb_2Se_3 films on ITO substrates were produced though varying the deposition temperature or coating 5 nm amorphous Sb_2Se_3 film on the substrate before RTE process. As shown in **Figure 2**a-c, the dominant diffraction peaks for the three Sb_2Se_3 films were (020), (120) and (221), and the corresponding preferred orientations were [020], [120] and [221], respectively. We call them as [020]-, [120]- and [221]-Sb_2Se_3 for short. Figure 2b-d present the cross-sectional scanning electron microscopy images of these three films. The vertical dimension of the Sb_2Se_3 grains approximate to the thickness of Sb_2Se_3

films, suggesting carriers largely travel within a single grain during TOF measurement. As a result, the TOF derived mobility from Sb_2Se_3 films of different orientation could fully reflect the mobility anisotropy in that the possible interference caused by scattering at the grain boundaries (GBs) is minimized. Figure 2e-g show the resultant normalized transient currents at various driving voltages on a bilogarithmic scale. The τ_t at various bias were determined by the intercept of the pre-transit and post-transit asymptotes of the photocurrent and marked by solid blue circles. The plots of $\tau_t \sim V^{-1}$ were plotted in the insets of Figure 2e-g. Combining the slopes of $\tau_t \sim V^{-1}$ and the thickness of the [020]-, [120]- and [221]-Sb_2Se_3 films (read from Figure 2b-d as 2.8, 3.0 and 3.1 μm, respectively), the hole mobilities calculated by Equation (2) for [020]-, [120]- and [221]-Sb_2Se_3 were 0.69, 0.81 and 1.25 $cm^2V^{-1}s^{-1}$, respectively.

Now, we discuss the carrier transport in [020]-, [120]- and [221]-Sb_2Se_3. Figure 2h-j shows the (020), (120) and (221) crystal plane of Sb_2Se_3 crystal. The solid azure lines stand for the carrier transport in covalent bond, and the red and green dash lines represent the carrier hopping from one ribbon to the adjacent ones along a- and b-direction, respectively. The shortest hopping distance along a- and b-direction are 3.29 Å and 3.64 Å, respectively (see supporting information), and therefore the hole mobility along the a-direction is expected to be larger than that along b-direction. Since the mobility obtained from [020]-Sb_2Se_3 was $\mu_{h,b}$ (the hole mobility along b-direction, similar to $\mu_{h,a}$ and $\mu_{h,c}$), and the mobility for [120]-Sb_2Se_3 should lie between $\mu_{h,b}$ and $\mu_{h,a}$, we thus believe for mobility along a random direction, the following equation should hold:

$$\frac{h^2}{h^2+k^2+l^2}\mu_a^2+\frac{k^2}{h^2+k^2+l^2}\mu_b^2+\frac{l^2}{h^2+k^2+l^2}\mu_c^2=\mu^2[hkl] \quad (3)$$

where h, k and l are orientation index, $\mu_{h,a}$, $\mu_{h,b}$ and $\mu_{h,c}$ are the hole mobility along a-, b- and c-direction, respectively. Equation (3) could be derived through decomposing mobility as a vector. Substituting [020], [120] and [221] into Equation (3), and solving the system of linear equations, we could obtain the mobility along a-, b- and c-direction as 1.17, 0.69 and 2.59 $cm^2V^{-1}s^{-2}$, respectively. $\mu_{h,c}$ is naturally the largest since this represents transport within the covalent bonded along Sb_2Se_3 ribbon, and $\mu_{h,a}$ is larger than $\mu_{h,b}$ as the distance that carriers have to hop is larger along the b-direction. These results reinforce our previous results[5], that indicate for photovoltaic applications, the best Sb_2Se_3 absorber is orirented [001] oriented. In addition, we meaured the conductivities of [020]-, [120]- and [221]-Sb_2Se_3 from current-voltage profiles. . Combining the conductivities and mobility, we calculated the free carrier density of our Sb_2Se_3 film as 1.8×10^{13} cm^{-3}, a value that is far below the optimal doping density of ~10^{16} cm^{-3} for photovoltaic absorber layer. This is also the reason why Hall measurements on our RTE processed Sb_2Se_3 films always fail.

Despite non-favorable film properties at room temperature, we found that measurements at elevated temperature thermally excited enough carriers to make the measurement. At 380 K, Sb_2Se_3 is dominated by “intrinsic excitation” (discussed below), and the mobility obtained from Hall measurement is $|\mu_e-\mu_h|$ (please refer to supporting information for detailed discussion). By repeating the Hall measurement at 380 K 10 times, the resultant average $|\mu_e-\mu_h|$ values for [020]-, [120]- and [221]-Sb_2Se_3 were 24.1±2.3, 12.1±2.1, and 8.9±1.9 cm^2 V^{-1} s^{-1}, respectively.

Assuming the mobility is mainly affected by acoustic scattering, the mobility is proportional to $T^{-3/2}$. The Hall mobilities at room temperature (298 K) for [020]-, [120]- and [221]-Sb_2Se_3 were 16.9, 8.5, and 6.2 $cm^2\ V^{-1}\ s^{-1}$, respectively. One needs to note that the mobility obtained from the Hall effect is along the vertical direction of [020], [120] and [221]. Thus, it was difficult to derive the electron mobility along the a-, b- and c-directions from the calculated hole mobility. But we can know that the electron mobility along c-direction is larger than 14.3 $cm^2\ V^{-1}\ s^{-1}$ (16.9 minus 2.59 $cm^2\ V^{-1}\ s^{-1}$) at room temperature. Moreover, the measured negative hall coefficient indicates that the electron mobility is larger than hole mobility which is consistent with our experiment result.

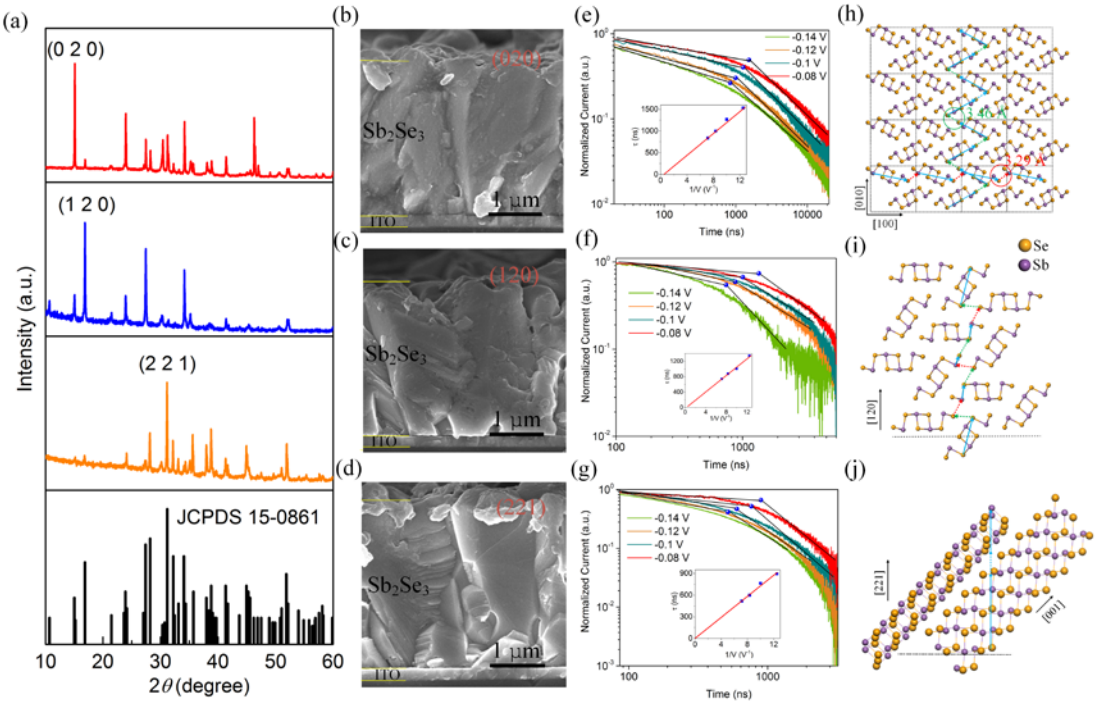

Figure 2. a) The X-ray diffraction patterns of [020]-, [020]- and [020]-Sb_2Se_3 films. The cross-sectional SEM image of b) [020]-Sb_2Se_3, c) [020]-Sb_2Se_3 and d) [020]-Sb_2Se_3 films. The transient current in TOF measurement of e) [020]-Sb_2Se_3, f) [020]-Sb_2Se_3 and g) [020]-Sb_2Se_3 films after photoexcitation at time t=0 in a

bilogarithmic plot; the transit time τ_t is identified as the crossover point of two blue lines. The crystal face h) (020), i) (120) and j) (221) of Sb_2Se_3. It is composed of one dimensional $(Sb_4Se_6)_n$ ribbons with orthorhombic crystal structure. The red and green dash arrows represent the carrier hopping from one ribbon to the adjacent ones along a- and b-direction, respectively. The azure solid arrows stand for carrier transporting within covalent bond.

2.3 Carrier dynamics and lifetime

We applied time-resolved femtosecond (fs-TA) and nanosecond (ns-TA) transient absorption spectrum to study the dynamics of photogenerated carriers in Sb_2Se_3 thin films. The description of the experimental setup can be found in a previous publication.[16] In the current work, the sample was pumped at 500 nm and probed at near-IR region (800-1300 nm). Because the pump photon energy is significantly higher than bandgap (1.17 eV),[3] the charge carriers initially created should be hot carriers. **Figure 3a** shows TA spectral evolution with respect to delay time. At short delay (0.3 ps, blue trace), a sharp photo-induced absorption (PIA) band peaks at 900 nm, which quickly evolves to dispersive line shape (3 ps, green trace). The PIA is attributed to the hot carrier induced band gap renormalization,[17] and then the fast spectral evolution implies the short intraband relaxation. The dispersive TA spectrum is also observed in other indirect bandgap semiconductors (e.g. multi-layer MoS_2), in which the photon-induced bleach and absorption were attributed to band-filling and transition broadening，respectively，by thermalized carriers at direct (or indirect) conduction band edge.[18] As the delay increases, the dispersive line shape evolves to a broad PIA band extends from 800 nm to >1300nm (300 ps, red traces), and this process is relatively slow, on the time scale of ~100 ps. The broad PIA band is attributed to the spectral shift in the presence of carriers in shallow trapped states.

Within 5 ns, the broad PIA band stops evolving, suggesting the long lifetime of the carriers at shallow trap states. The three-phase dynamics is more clearly shown by the TA kinetics averaged between 900 and 950 nm (Figure 3b, phase I, II, and III). To monitor the depopulation of the trapped carriers due to charge recombination, the kinetics of the broad PIA band is also measured on the nansecond timescale, which is shown in Figure 3c. The carrier lifetime is determined to be ~67 ns by the exponential fit.

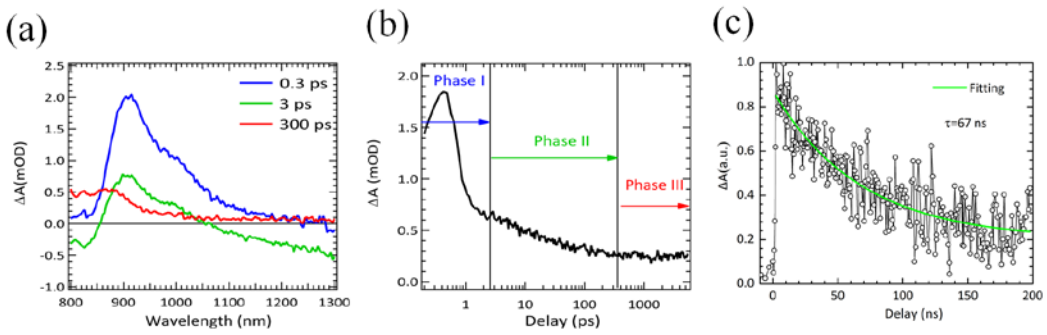

Figure 3. a) TA spectrum at various time delays after photoexcitation. b) Fs-TA kinetics averaged between 900 and 950 nm. c) Ns-TA edge kinetics averaged between 900 and 950 nm and the corresponding single exponential fitting (green lines) for Sb_2Se_3 film.

2.4 Diffusion length

Our RTE derived Sb_2Se_3 thin film is weakly p-type, and the minority carrier (electron) diffusion length along c-direction, $L_{e,c,}$ is a parameter that heavily influences photovoltaic performance. $L_{e,c}$ can be estimate by Equation (4):

$$L_{e,c} = \sqrt{\frac{D_{e,c}T}{q}} = \sqrt{\frac{\mu_{e,c}\tau_e k_B T}{q}} \quad (4)$$

where $D_{e,c}$ is the electron diffusion coefficient along c-direction, $\mu_{e,c}$is electron mobility along c-direction, k_B is the Boltzmann constant, T is the absolute temperature, q is the elementary charge, and τ_e (67 ns) is the electron lifetime. From the mobility

(14.3 cm^2/V-s) and lifetime (67 ns) parameters, we obtain the electron diffusion length of 1.6 μm along c-direction. Since both the electron lifetime and mobility are strongly carrier-density dependent, and both the TA and TOF measurement were carried out under high illumination, we believe as-calculated diffusion length is valid only under strong irradiation. We thus further applied the bias voltage dependent internal quantum efficiency (IQE) to deduce the diffusion length under weak light illumination (xenon lamp spectrum of ~150 μW/cm^2 during IQE measurement).[19] The device structure for extracting diffusion length is ITO/CdS/Sb_2Se_3/Au (inset in **Figure** 4a) with efficiency of 5.4% (Voc=0.391 V, Jsc= 25.2 mAcm^{-2} and FF=54.7%). Extraction from this technique was done using the following steps in sequence: (1) measuring EQE(λ,V) as a function of wavelength (λ) at a series of voltage bias (V); (2) determining the reflectivity R(λ) and transmittance T(λ) as a function of wavelength; (3) calculating internal quantum efficiency, IQE(λ,V) using the relation of IQE(λ,V)=EQE(λ,V)/[1-R(λ)-T(λ)]; (4) obtaining the voltage dependence of depletion width x_d(V) from capacitance-voltage (C-V) measurement; (5) obtaining the dependence of x_d on IQE at each λ; (6) extracting diffusion length and absorption coefficient (α) from the expression given by Equation (5).[20]

$$-\ln(1-IQE) = \alpha x_d + \ln(1+\alpha L_e) \qquad (5)$$

Equation (5) is valid only when all carriers generated within the depletion region are collected with 100% probability while the carriers generated in the quasi-neutral region are collected with an exponentially decaying probability with the length scale, defined by the minority carrier diffusion length. In our device, the thickness of Sb_2Se_3

was 530 nm, and the depletion width was approximately 193 nm obtained from *C-V* measurement, which meant that the quasi-neutral region was about 337 nm where photogenerated carriers are collected by diffusion. The IQE at 500-700 nm range was nearly 100%, thus validating our assumption of 100% carrier collection efficiency in the depletion region. The plot of Equation (5) is shown in Figure 4a. The extracted diffusion length of minority carrier (electron) was about 285 nm under xenon lamp illumination with an intensity of 150 μWcm^{-2} And the direction of diffusion length was corresponding to the orientation of Sb_2Se_3 as (221). To test our assumptions and thus lend credibility to our result, we verified consistency between e calculated absorption coefficient derived from EQE and CV (Figure 4b).. We thus conclude that depending on the illumination intensity, the carrier diffusion length within our RTE produced Sb_2Se_3 film is between 285 nm and 1.6 μm.

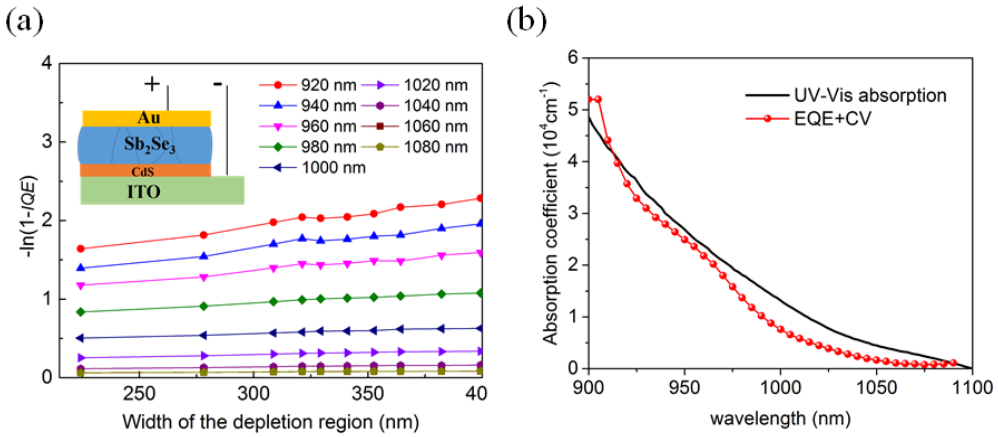

Figure 4. Estimation of diffusion length by the bias dependent IQE method. a) -ln(1-IQE) against depletion width. The diffusion length and absorption coefficient were extracted by the intercept and slope of the linear fitting. b) Comparison between the absorption coefficient derived from EQE+CV (red dots line) and the measured value from transmission (black line).

2.5 Defect depth

Temperature dependent dark conductivity was measured to investigate defect

types and depths in our Sb_2Se_3 thin films. We used a symmetric device structure ,Au/Sb_2Se_3/Au (as the inset in Figure 3a), with glass as the substrates and Au electrodes with a spacing of 200 μm as the Ohmic contacts. Resistances were evaluated around the zero bias voltage from *I-V* data by linear least-square fitting.

The conductivity of Sb_2Se_3 film at 85 to 420 K was in the order of 10^{-4} to 10^{-11} S cm^{-1} (see **Figure** 5a). We identify two different transport mechanisms. At high temperatures (above 160 K), the electrical conductivity depends on the number of carriers thermally activated from the defects to the band, which again depend on defect depth and temperature, as shown in Equation (6):[21]

$$\sigma = \sum_{n=1,2...} \sigma_n \exp\left(-\frac{E_n}{k_B T}\right) \quad (6)$$

where E_n is the activation energies and σ_n is the pre-exponential factor, k_B is Boltzmann constant and T is the absolute temperature. Figure 5a shows the plot of $\ln(\sigma)$ against $1000/T$. Two linear regions were observed, so we use n=2 here, and the corresponding activation energies were obtained by fitting Equation (6). Between 250 and 420 K, the activation energy E_1 is 0.578 eV, which is approximately half of the direct band gap (1.17 eV) of Sb_2Se_3. Obviously, in this temperature region, intrinsic excitation dominates the carrier density. Between 160 and 250 K, the fitted activation energy E_2 was 0.111 eV, corresponding to a defect depth of 0.111 eV. This defect is ascribed to the acceptor defect of Se_{Sb} as suggested by theoretical calculation that Se_{Sb} has the lowest formation energy and is a shallow acceptor with defect depth of approximately 0.1 eV.[22] In the low temperature region (85-160 K), the conductivity is slowly reduced with the temperature because the conduction mechanism change

into Mott's variable range hopping between localized states. The conductivity as a function of temperature is described in Equation (7):[23]

$$\sigma(T) = \sigma_0' T^{-1/2} \exp\left[-(T_0 / T)^{1/4}\right] \quad (7)$$

where T_0 is a characteristic temperature which is related to the disorder of the material. σ_0' is a constant. Figure 5b shows the plot of $\ln(\sigma T^{1/2})$ against $T^{1/4}$. It is clear that the relation is linear, which indicates the occurrence of a hopping conduction mechanism and from which we can calculate the characteristic temperature T_0 as 2.31×10^6 K. This value is larger than the values of CZTS and CIGS,[24] implying worse ordering in our Sb_2Se_3 film possibly due to their one dimensional crystal structure giving rise to more disordering.

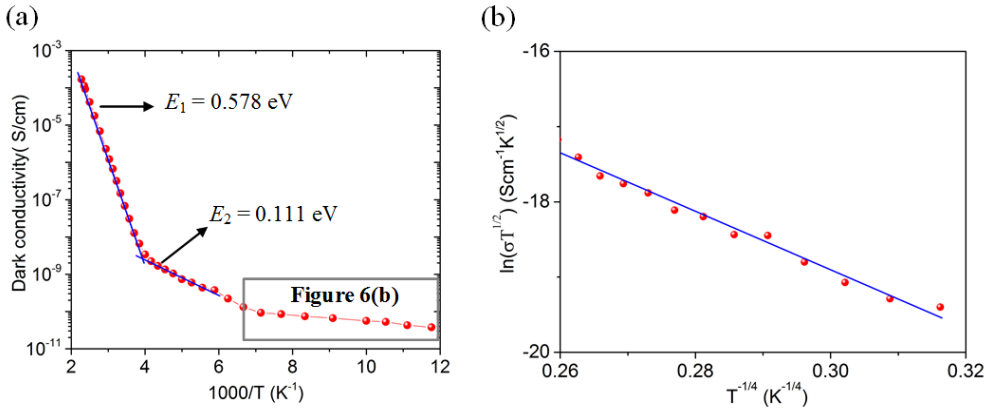

Figure 5. Defect characterization by temperature dependent conductivity measurement. a) Logarithmic dark conductivity versus $1000/T$ in the temperature range of 85 to 420 K; b) $\ln(\sigma T^{1/2})$ versus $T^{1/4}$ in the temperature range of 85 to 160 K.

2.6 Density of defect states

As discussed above, we believe shallow acceptor Se_{Sb} were the dominant defects in our Sb_2Se_3 films produced by RTE. Using the T. Walter's method,[25] we could extract the density of defect states from thermal admittance spectroscopy (TAS). Device configuration for TAS measurement was ITO/CdS/Sb_2Se_3/Au as the inset in

Figure 4a, our standard superstrate solar cell configuration. The experiments were performed using Keithley 4200-CVU module with frequencies ranging from 1 kHz to10 MHz. The energy profile of trap density of states (N_t) can be derived from the angular frequency dependent capacitance with the Equation (8):[25]

$$N_t\left(E_\omega\right) = -\frac{V_{bi}}{qx_d}\frac{dC}{d\omega}\frac{\omega}{k_B T} \tag{8}$$

where C is the capacitance, ω is the angular frequency ($\omega = 2\pi f$), q is the elementary charge, k_B is the Boltzmann constant and T is temperature. V_{bi} and x_d are the built-in potential and depletion width, respectively, which were extracted from the Mott-Schottky analysis. The applied angular frequency ω defines an energetic demarcation as Equation (9):[25]

$$E_\omega = k_B T \ln\left(\frac{\omega_0}{\omega}\right) \tag{9}$$

where E_ω is the energy depth of the defect relative to the corresponding band edge, ω_0 is the attempt-to-escape frequency which is related to defect capture cross section, effective density of states in the valence band, and thermal velocity. **Figure** 6a is the density of defect states. There was a Gaussian defect peak in the gap with the peak position at 0.095 eV, which was consistent with the defect depth of 0.111 eV obtained from temperature dependent conductivity measurement. The profile of the defect distribution is shown in Figure 6b. The density of defect states was about 10^{16} $cm^{-3}eV^{-1}$ at the peak position and the integrated defect density was 1.3×10^{15} cm^{-3}.

The defect density could also be extracted from space charge limited current (SCLC) measurement at the transition regime between the linear region and the quadratic

region (as seen in supporting information).[26] The trap density n_t was 6.9×10^{14} cm^{-3} based on the SCLC result, in good agreement with the value obtained from TAS. We should emphasize that our first-principle calculation using VSAP code also predicted an equilibrium defect density of 1×10^{15} cm^{-3} for Sb_2Se_3 film at room temperature,[22] thus validating our experimental results. Assuming the probability of defect activation dictated by the Fermi-Dirac distribution as $1/[1+\exp[(E_t-E_F)/kT]]$, the activated percentage of defects would be 3.4% corresponding to the extremely low doping density of 2.4×10^{13} cm^{-3}, echoing our previous carrier density measurement.

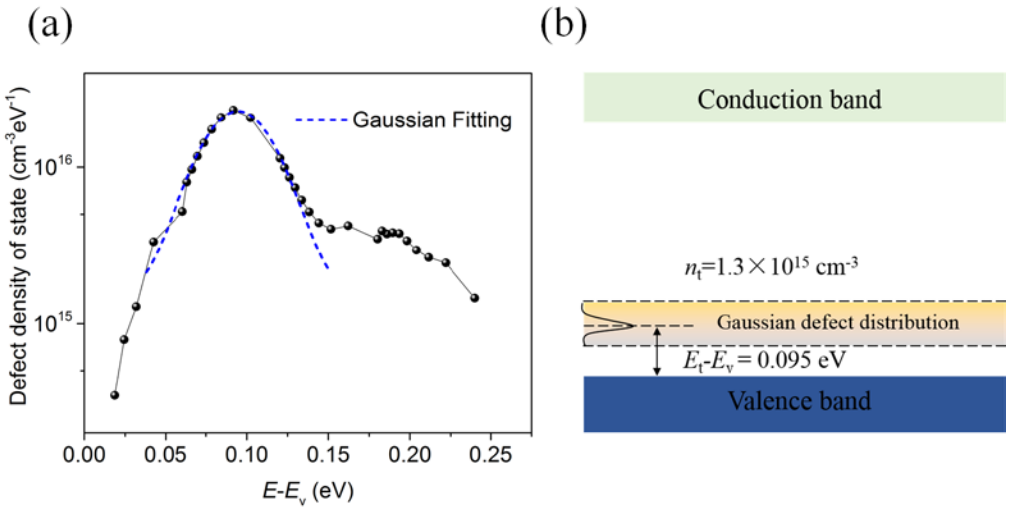

Figure 6. Defect distribution in Sb_2Se_3 film. a) The density of defect states of Sb_2Se_3 from admittance spectra. The defect peak at 0.095 eV could be perfectly fitted by Gaussian function as blue dash line. b) The Gaussian defect distribution in the band gap.

2.7 Optical Band tail

Band tails in the optical absorption band edges are observed in many disorder materials. For photovoltaic applications, the local band tail state can lead to the degradation of device performance particularly for V_{OC}. It can be caused by doping or disorder due to the destruction of the lattice periodicity. The band tail can be investigated by photothermal deflection spectroscopy (PDS), which is widely used to

examine the optical properties of materials. The devices for PDS measurement were prepared by depositing 1000 nm c-Sb_2Se_3 films on quartz glass using RTE. PDS spectra were acquired from 0.6 to 2.5 eV, and were subsequently repeated over the course of several days. We found no appreciable change in the PDS signal, thus verifying the stability of these materials against the index fluid, perfluorohexane. The detailed test process is shown in experiment section. We obtained absorption coefficients by first system correcting the raw data using a "blackbody" spectrum from a graphite thin film painted on glass substrates identical to those used for sample growth. We then scaled the PDS spectra to make the above gap data consistent with absorptance, $A = 1 - R - T$ (R and T represent reflectance and transmittance, respectively), data that was obtained with a Cary 2500 and integrating sphere. Lastly we converted the absorptance to absorption coefficient using Equation (10), neglecting reflections from the film-substrate interface,[27]

$$\alpha(\mathrm{cm}^{-1}) = \frac{1}{d}\ln\left(1+\frac{A}{T}\right) \qquad (10)$$

where d is the sample thickness. The PDS spectrum were shown in **Figure 7**. The Urbach energy was estimated from fitting the exponential band-edge portion of the absorption coefficient versus energy plot by Equation (11).[28]

$$\alpha(h\nu) = \alpha_0 \exp\left[(h\nu - U_1)/U_0\right] \qquad (11)$$

where $h\nu$ is the photon energy, U_0 is the Urbach energy, U_1, and α_0 are constants determined by fits to experiment. In the energy range of 1.1 to 1.25 eV, the Urbach energy is around 40 meV. Another extremely large Urbach energy (~120 meV) was observed in lower energy region (0.8 to 1.1 eV) in the crystal Sb_2Se_3 spectra. These

unsually large Urbach energies may result not from the Sb2Se3 film, but from other non-stoichiometric phases in the film that occur during growth in non-optimal conditions.For example, the presence of oxygen during growth may consume antimony and leave selenium rich regions, which are more disordered. These observations (i.e. antimony oxides, etc..) help explain the low device performance for our Sb_2Se_3 solar cells, and motivate further optimization of growth conditions

To test this speculation, we measured the PDS spectra of amorphous Sb_2Se_3 film (black dots in Fig 7) which was completely disordered and then compared it to the crystalline counterparts (red dots in Fig 7). A-Sb_2Se_3 film was deposited by thermal evaporation (TE) with the substrate at room temperature. The a-Sb2Se3 PDS spectra showed only one exponential region with Urbach energy ~ 80 meV, while in the crystalline samples, the large Urbach energy region begins near 1 eV

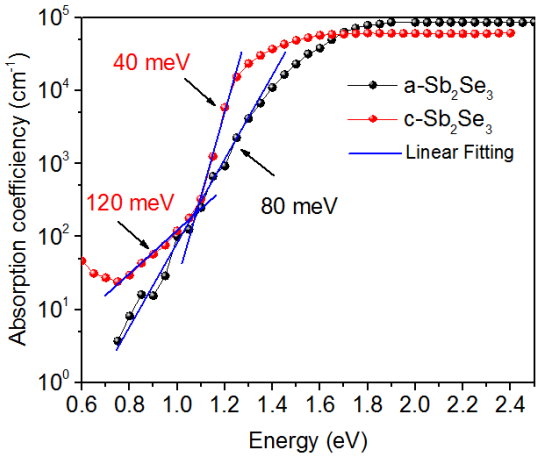

Figure 7. Absorption coefficient vs. Energy. The Absorption coefficient of crystal and amorphous Sb_2Se_3 films were obtain from PDS spectrum.

3. Discussion

We now discuss the cons and pros of our Sb_2Se_3 thin films in terms of optoelectronic properties, as well as the suggested strategies for further efficiency improvement based on our characterization.

First, we argue that pseudo-direct optical transition nature of Sb_2Se_3 might be beneficial for photovoltaic application. For our Sb_2Se_3, the lowest indirect band gap (E_{ind}) is 1.04 eV and the lowest direct band gap (E_d) is 1.17 eV at room temperature, which means Sb_2Se_3 absorption starts at 1192 nm and then changes to strong absorption at 1060 nm due to the p->p transition[29] and direct band gap. Presently, absorption is not a limiting factor, as J_{SC} of 25 $mAcm^{-2}$ was obtained in our certified device with the Sb_2Se_3 absorber of only 390 nm thickness. One natural advantage of pseudo-direct band gap is the long carrier lifetime owning to the phonon-assisted recombination nature. The TA derived carrier lifetime is 67 ns, which is shorter than $CH_3NH_3PbI_3$ (288 ns from TA measurement)[30] and the best CdTe single crystals (400 ns, single-photon counted decay),[31] but significantly longer than CZTSSe (6.7 ns measured from photoluminescence decay)[32], CIGS (5.5 ns measured from photoluminescence decay)[33] and SnS (<100 ps measured from transient terahertz photoconductivity)[34]. One further advantage associated with high absorption coefficient and long carrier lifetime is that Sb_2Se_3 can maintain high non-equilibrium carrier density under AM1.5G illumination, thus permitting large Fermi level splitting and higher open circuit voltages.

Second, we discuss the implication of the measured mobility of our Sb_2Se_3 film. The along-ribbon mobility of Sb_2Se_3 lies in 1-20 $cm^2\ V^{-1}\ s^{-1}$, better than PbS CQDs (0.001-0.1 $cm^2\ V^{-1}\ s^{-1}$),[35] Cs_2SnI_6 (2.9 $cm^2\ V^{-1}\ s^{-1}$)[36] and $CuZnSn(S,Se)_4$ (0.5-1.3 $cm^2\ V^{-1}\ s^{-1}$)[37] yet worse than Bi_2S_3 (257 $cm^2\ V^{-1}\ s^{-1}$)[38], $CH_3NH_3PbI_3$ (15-40 $cm^2\ V^{-1}\ s^{-1}$)[39] and SnS (128 $cm^2\ V^{-1}\ s^{-1}$).[40] Mediocre carrier mobility in combination with the

better-than-average carrier lifetime results in a decent diffusion length approaching 1.6 μm under strong light illumination, which is much better than PbS CQDs solid which has strived for >300 nm diffusion length for years and now has obtained certified device efficiency of 10.7%.[41] The concern is the highly anisotropic nature of mobility due to its one dimensional crystal structure. Stringent control of c-axis oriented film is imperial for high efficiency thin film solar cells, and preliminary success was obtained through deposition temperature control.

Last we would discuss the defects and doping density in Sb_2Se_3. Previous theoretical simulation, and the present experimental results included here suggest that the dominant defect in Sb_2Se_3 film produced by RTE strategy is Se_{Sb} acceptor with defect depth of ~0.1 eV and density of ~1×10^{15} cm^{-3}. Defect depth is acceptable yet more shallow defects such as V_{Cu} in CIGS with a depth of ~0.03 eV is preferable. The doping density is far lower than the optimal value of approximately 10^{16} cm^{-3} for the absorber layer in a photovoltaic device. Whether this is intrinsic for this material, or it is because of the strong compensation by defect pairs remains elusive at this stage. Strategies to significantly increase carrier density in Sb_2Se_3 film deserve further efforts. Alternatively, construction of device with p-i-n configuration, in analogy to HIT silicon or perovskite solar cell, would probably circumvent this obstacle. In addition, the large band tail in our Sb_2Se_3 films is harmful to solar cells. However, it may be overcome by supplementing Se element, increasing the crystallinity and eliminating the different phase such as Sb_2O_3.

Table I. The summary of physical parameters of Sb_2Se_3 reported in this paper.

Parameter		Our value	Characterization method
ε_r		18	CF, 2 MHz
		29	CF, 2 kHz
μ_h [$cm^2 V^{-1} s^{-1}$]	a	1.17	TOF
	b	0.69	
	c	2.59	
μ_e [$cm^2 V^{-1} s^{-1}$]	c	>14.3	Hall effect
τ_e [ns]		67	TA
L_e [μm]	[221]	0.285	Bias IQE, low illumination
	[001]	1.6	Calculated, high illumination
p [cm^{-3}]		1.8×10^{13}	IV
n_t [cm^{-3}]		6.9×10^{14}	SCLC
		1.3×10^{15}	TAS
E_t-E_v [eV]		0.095	TAS
E_1 [eV]		0.578	Conductivity
E_2 [eV]		0.111	Conductivity
T_0 [K]		2.31×10^{6}	Conductivity
U_0 [meV]	c-Sb_2Se_3	40	(1.1-1.25 eV) PDS
	c-Sb_2Se_3	120	(0.8-1.1 eV) PDS
	a-Sb_2Se_3	80	(0.8-1.25 eV) PDS

4. Conclusion

The dielectric constant of Sb_2Se_3 is between 29 to 18 with the frequency 2 kHz-2 MHz. The hole mobility in a single Sb_2Se_3 grain along a-, b- and c-direction were 1.17, 0.69 and 2.59 $cm^2V^{-1}s^{-2}$, respectively. The electron mobility along c-direction was larger than 16.9 $cm^2 V^{-1} s^{-1}$. Fs-TA and ns-TA spectrum gave the minority carrier lifetime was 67 ns. The electron diffusion length along c-direction under high illumination was 1.6 μm, while under low illumination along [221] the electron diffusion length was 285 nm. The temperature dependent dark conductivity indicated two thermal activation energies were 0.578 eV at high temperature and 0.111 eV at

medium temperature and the transport mechanism changed to variable range hopping at low temperature. TAS was used to determine the density of defect states in the order of magnitude 10^{16} $cm^{-3}eV^{-1}$ and the position of defect peak at 0.095 eV. The corresponding integrated defect density is 1.3×10^{15} cm^{-3} which is in good agreement with that of 6.9×10^{14} cm^{-3} obtained from SCLC. The free carrier density was about 1.8×10^{13} cm^{-3}. The Urbach energy of c-Sb2Se3 is 40 meV in the range of 1.1 to 1.25 eV and 120 meV in the range of 0.8 to 1.1 eV. While the Urbach energy of a-Sb_2Se_3 is 80 meV in the range of 0.8 to 1.25 eV.

In brief, the reasonably good optoelectronic properties revealed here, coupled with its excellent material properties such as simple and stable phase, non-toxic and low-cost constituents, rendering our Sb_2Se_3 stands out among many emerging absorber materials and thus deserving further extensive study.

5. Experimental Section

Martials preparation: Sb_2Se_3 films were prepared using rapid thermal evaporation (RTE). The procedure detail could be found elsewhere.[5] The film with different thickness were realized by change the evaporation time. Au electrode was fabricated by thermal evaporation.

Sb_2Se_3 solar cells fabrication: Glass/ITO/CdS/Sb_2Se_3/Au devices were used for biased IQE and TAS measurement. The substrate is In-doping tin oxide (ITO)-coated glass. CdS buffer layer was deposited by chemical bath deposition (CBD) with the thickness about 60 nm. Sb_2Se_3 absorption layer and Au electrode were produced as

mentioned above.

Materials characterization: Film morphology was characterized using scanning electron microscopy (SEM) (FEI Nova NanoSEM450 microscope). XRD was applied to characterize the structures of Sb_2Se_3 thin films. Measurement was carried out on Philips diffractometer (X pert pro MRD using Cu Kα radiation. The standard diffraction pattern of Sb_2Se_3 is JCPDS 00-015-0861.

TOF measurement: Measurements were carried out in an optically and electrically shielded box at room temperature. TOF measurements were performed on a Keithley 2400 as the power source and an Agilent infiniium DSO 8104A oscilloscope for acquiring the transient signal. Monochromatic light excitation was provided by a pulsed laser at the wavelength of 532 nm from ITO. Pulse of 78 ps length at a frequency of 1 KHz were produced. In order to confirm the results, two set of Sb_2Se_3 films with different orientation were studied, and the results agreed with each other very well.

TA measurement: The 400 nm thick Sb_2Se_3 film for TA measurement was fabricated by RTE on quartz substrate. The femtosecond and nanosecond TA measurements were conducted in the broadband pump-probe TA spectrometers (Helios and Eos from Ultrafast Systems, LLC). The probe (800-1400 nm) and pump (500 nm) are generated through non-linear optical processes based on a fundamental pulsed laser beam provided by a Ti:Sapphire amplifier with integrated oscillator and pump laser. The wavelength and temporal width of the fundamental pulse are 800 nm and ~130 fs, respectively.

Biased IQE measurement: Before IQE measurement, we carried out transmission and reflection spectrum using Lambda 950 (Perkin Elmer). For external quantum efficiency (EQE) measurement, light source was generated by a 300W xenon lamp of Newport (Oriel, 69911) and then split into monochromatic light using Newport oriel cornerstone^{TM} 130 1/8 Monochromator (Oriel, model 74004). A reference standard silicon solar cell was used for calibration. A Keithley 2400 source meter was used to apply bias.

Temperature dependent conductivity: I-V measurements in the temperature range of 80-420 K were performed on an Agilent B1500A in dark condition. A liquid nitrogen cryostat (Variable Temperature Insert Cryostat, CRYO Industries of America Inc.) was used to regulate temperature.

PDS measurement: The PDS measurements were made in transverse mode,[42] using reflective optics to guide the pump beam from a single grating monochromator to a sample. The pump beam was chopped at 6 Hz and was focused to a spot size of approximately 1 mm.[27] The samples were kept in a helium purged glove box, until time of measurement, when they were loaded into a quartz cuvette and immersed in anhydrous perfluorohexane. The probe beam consisted of ~2 mW, 633 nm laser light from an intensity stabilized helium-neon laser. Alignment of the probe beam was made using a 3 axis stage and care was taken to avoid sample illumination from the probe beam. Probe beam deflections measured by a silicon photo-diode were amplified and processed using lock-in methods.

Supporting Information

Supporting Information is available from the Wiley Online Library or from the author.

Acknowledgements

This work was supported by the National Key Research and Development Program of China (2016YFA0204000), the National Natural Science Foundation of China (NSFC 61322401, 91433105) and the director fund of Wuhan National Laboratory for Optoelectronics, the Fundamental Research Funds for the Central Universities, HUST (2016JCTD111) and the Special Fund for Strategic New Development of Shenzhen, China (JCYJ20160414102210144) and "National 1000 Young Talents" project. Professor Shiyou Chen at East China Normal University is acknowledged for helpful discussions. The authors would like to thank the Analytical and Testing Center of HUST and the Center for Nanoscale Characterization and Devices of WNLO for the characterization support.

Received: ((will be filled in by the editorial staff))
Revised: ((will be filled in by the editorial staff))
Published online: ((will be filled in by the editorial staff))

[1] J. Petzelt, J. Grigas, Ferroelectrics **1973**, 5, 59.

[2] Y. Zhou, M. Leng, Z. Xia, J. Zhong, H. Song, X. Liu, B. Yang, J. Zhang, J. Chen, K. Zhou, J. Han, Y. Cheng, J. Tang, Adv. Energy Mater. **2014**, 4, 1301846.

[3] C. Chen, W. Li, Y. Zhou, C. Chen, M. Luo, X. Liu, K. Zeng, B. Yang, C. Zhang, J. Han, J. Tang, Appl. Phys. Lett. **2015**, 107, 043905.

[4] G. Ghosh, J. Phase Equilib. **1993**, 14, 753.

[5] Y. Zhou, L. Wang, S. Chen, S. Qin, X. Liu, J. Chen, D.-J. Xue, M. Luo, Y. Cao, Y. Cheng, E. H. Sargent, J. Tang, Nat. Photonics **2015**, 9, 409.

[6] a) M. Luo, M. Leng, X. Liu, J. Chen, C. Chen, S. Qin, J. Tang, Appl. Phys. Lett. **2014**, 104, 173904; b) X. Liu, J. Chen, M. Luo, M. Leng, Z. Xia, Y. Zhou, S. Qin, D.-J. Xue, L. Lv, H. Huang, ACS Appl. Mater. Inter. **2014**, 6, 10687; c) M. Leng, M. Luo, C. Chen, S. Qin, J. Chen, J. Zhong, J. Tang, Appl. Phys. Lett. **2014**, 105, 083905; d) X. Liu, C. Chen, L. Wang, J. Zhong, M. Luo, J. Chen, D.-J. Xue, D. Li, Y. Zhou, J. Tang, Prog. Photovoltaics: Res. Appl. **2015**, 23, 1828.

[7] P. Sinsermsuksakul, L. Sun, S. W. Lee, H. H. Park, S. B. Kim, C. Yang, R. G. Gordon, Adv. Energy Mater. **2014**, 4, 1400496.

[8] K. Maraun, Solar Frontier Achieves World Record Thin-Film Solar Cell Efficiency: 22.3%, http://www.solar-frontier.com/eng/news/2015/C051171.html, accessed: May, 2016.

[9] M. Osborne, First Solar pushes CdTe cell efficiency to record 22.1%, http://www.pv-tech.org/news/first-solar-pushes-cdte-cell-efficiency-to-record-22.1, accessed: May, 2016.

[10] W. Wang, M. T. Winkler, O. Gunawan, T. Gokmen, T. K. Todorov, Y. Zhu, D. B. Mitzi, Adv. Energy Mater. **2014**, 4, 1301465.

[11] a) J. Black, E. M. Conwell, L. Seigle, C. W. Spencer, J. Phys. Chem. Solids **1957**, 2, 240; b) S. L. Benjamin, C. H. de Groot, A. L. Hector, R. Huang, E. Koukharenko, W. Levason, G. Reid, J. Mater. Chem. C **2015**, 3, 423.

[12] J. Ma, T. Su, M.-D. Li, W. Du, J. Huang, X. Guan, D. L. Phillips, J. Am. Chem. Soc. **2012**, 134,

14858.
[13] O. Madelung, *Semiconductors: data handbook*, Springer Science & Business Media, New York, USA **2012**.
[14] M. Engel, F. Kunze, D. C. Lupascu, N. Benson, R. Schmechel, Phys. Status Solidi-R. **2012**, 6, 68.
[15] J. R. Haynes, W. Shockley, Phys. Rev. **1951**, 81, 835.
[16] Y. Yang, W. Rodríguez-Córdoba, T. Lian, J. Am. Chem. Soc. **2011**, 133, 9246.
[17] Y. Yang, D. P. Ostrowski, R. M. France, K. Zhu, J. van de Lagemaat, J. M. Luther, M. C. Beard, Nat Photon **2016**, 10, 53.
[18] H. Shi, R. Yan, S. Bertolazzi, J. Brivio, B. Gao, A. Kis, D. Jena, H. G. Xing, L. Huang, ACS Nano **2013**, 7, 1072.
[19] T. Gokmen, O. Gunawan, D. B. Mitzi, J. Appl. Phys. **2013**, 114, 114511.
[20] X. X. Liu, J. R. Sites, J. Appl. Phys. **1994**, 75, 577.
[21] J. Y. W. Seto, J. Appl. Phys. **1975**, 46, 5247.
[22] X. Liu, X. Xiao, Y. Yang, D.-J. Xue, D. Li, C. Chen, S. Lu, L. Gao, Y. He, B. M. C, G. Wang, S. Chen, J. Tang, Enhanced Sb_2Se_3 solar cell performance through theory-guided defect control 2016 (unpublished).
[23] N. F. Mott, E. A. Davis, *Electronic processes in non-crystalline materials*, OUP Oxford, OX2 6DP **2012**.
[24] B. L. Guo, Y. H. Chen, X. J. Liu, W. C. Liu, A. D. Li, AIP Adv. **2014**, 4, 097115.
[25] T. Walter, R. Herberholz, C. Müller, H. W. Schock, J. Appl. Phys. **1996**, 80, 4411.
[26] R. H. Bube, J. Appl. Phys. **1962**, 33, 1733.
[27] D. Ritter, K. Weiser, Opt. Commun. **1986**, 57, 336.
[28] F. Urbach, Phys. Rev. **1953**, 92, 1324.
[29] M. A. Tumelero, R. Faccio, A. A. Pasa, J. Phys. Chem. C **2016**, 120, 1390.
[30] S. D. Stranks, G. E. Eperon, G. Grancini, C. Menelaou, M. J. P. Alcocer, T. Leijtens, L. M. Herz, A. Petrozza, H. J. Snaith, Science **2013**, 342, 341.
[31] J. M. Burst, J. N. Duenow, D. S. Albin, E. Colegrove, M. O. Reese, J. A. Aguiar, C. S. Jiang, M. K. Patel, M. M. Al-Jassim, D. Kuciauskas, Nat. Energy **2016**, 1, 16015.
[32] T. K. Todorov, J. Tang, S. Bag, O. Gunawan, T. Gokmen, Y. Zhu, D. B. Mitzi, Adv. Energy Mater. **2013**, 3, 34.
[33] I. Repins, M. Contreras, M. Romero, Y. Yan, W. Metzger, J. Li, S. Johnston, B. Egaas, C. DeHart, J. Scharf, B. E. McCandless, R. Noufi, "Characterization of 19.9%-efficient CIGS absorbers", presented at *Photovoltaic Specialists Conference, 2008. PVSC '08. 33rd IEEE*, 11-16 May 2008, **2008**.
[34] R. Jaramillo, M.-J. Sher, B. K. Ofori-Okai, V. Steinmann, C. Yang, K. Hartman, K. A. Nelson, A. M. Lindenberg, R. G. Gordon, T. Buonassisi, J. Appl. Phys. **2016**, 119, 035101.
[35] J. Tang, K. W. Kemp, S. Hoogland, K. S. Jeong, H. Liu, L. Levina, M. Furukawa, X. Wang, R. Debnath, D. Cha, Nat. Mater. **2011**, 10, 765.
[36] B. Saparov, J.-P. Sun, W. Meng, Z. Xiao, H.-S. Duan, O. Gunawan, D. Shin, I. G. Hill, Y. Yan, D. B. Mitzi, Chem. Mater. **2016**, 28, 2315.
[37] K. F. Tai, O. Gunawan, M. Kuwahara, S. Chen, S. G. Mhaisalkar, C. H. A. Huan, D. B. Mitzi, Adv. Energy Mater. **2015**, 6, 1501609.
[38] H. Song, X. Zhan, D. Li, Y. Zhou, B. Yang, K. Zeng, J. Zhong, X. Miao, J. Tang, Sol. Energy Mater. Sol. Cells **2016**, 146, 1.
[39] Q. Dong, Y. Fang, Y. Shao, P. Mulligan, J. Qiu, L. Cao, J. Huang, Science **2015**, 347, 967.

[40] K. T. R. Reddy, N. K. Reddy, R. W. Miles, Sol. Energy Mater. Sol. Cells **2006**, 90, 3041.

[41] G.-H. Kim, F. P. García de Arquer, Y. J. Yoon, X. Lan, M. Liu, O. Voznyy, Z. Yang, F. Fan, A. H. Ip, P. Kanjanaboos, S. Hoogland, J. Y. Kim, E. H. Sargent, Nano Lett. **2015**, 15, 7691.

[42] W. B. Jackson, N. M. Amer, A. Boccara, D. Fournier, Appl. Opt. **1981**, 20, 1333.

1

Table of contents entry

We have systematically researched the basic physical properties of Sb_2Se_3 film such as dielectric constant, anisotropic mobility, carrier lifetime, diffusion length, defect depth, defect density and band tail. Mediocre carrier mobility in combination with the better-than-average carrier lifetime results in a decent diffusion length. Shallow acceptor Se_{Sb} dominates the defects with the defect depth of ~0.1 V and the defect density of ~1×10^{15} cm^{-3}.

Keywords: Sb_2Se_3, mobility, lifetime, defects

Chao Chen, Ye Yang, David C. Bobela, Shuaicheng Lu, Kai Zeng, Bo Yang, Liang Gao, Matthew C. Beard, Jiang Tang*

Characterization of Basic Physical Properties of Sb_2Se_3 and its relevance for photovoltaics

ToC figure

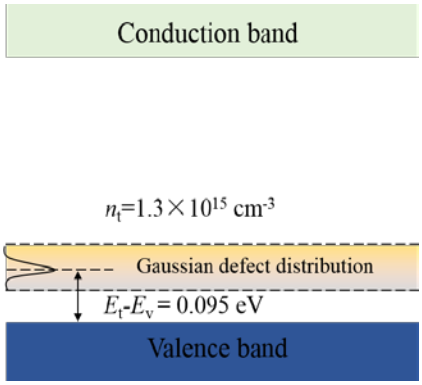

Supporting Information

Characterization of Basic Physical Properties of Sb_2Se_3 and its relevance for photovoltaics

*Chao Chen, Ye Yang, David C. Bobela, Shuaicheng Lu, Kai Zeng, Bo Yang, Liang Gao, Matthew C. Beard, Jiang Tang**

1. Atom distance

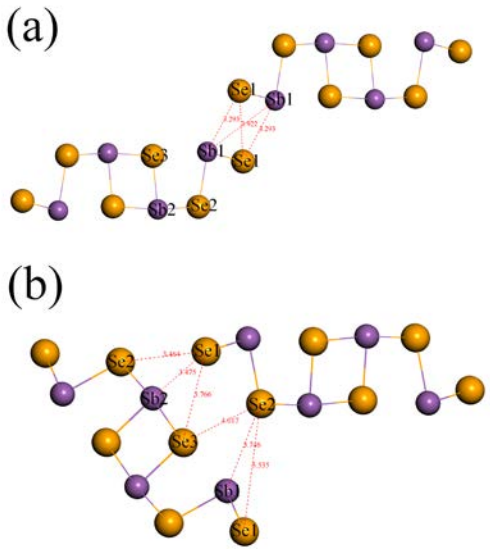

Figure S1. The atom distances of Sb-Sb, Sb-Se and Se-Se in Sb_2Se_3 crystal.

2. Space charge limited current (SCLC)

The defect density can be extracted from SCLC measurement at the transition regime between the linear region and the quadratic region by Equation (S1):[1]

$$n_t = \frac{2\varepsilon_r \varepsilon_0 V_{TFL}}{qd^2} \quad \text{(S1)}$$

where V_{TFL}=16.5 V is the turning point between linear and non-linear regime representing the onset voltage of the trap filled limit (TFL) as shown in Figure S2. ε_0 is the vacuum permittivity, ε_r=29 is the dielectric constant of Sb_2Se_3 at low frequency, q is the elementary charge, n_t is the trap density and d is the thickness of Sb_2Se_3. The trap density n_t was 6.9×10^{14} cm^{-3} based on the SCLC result.

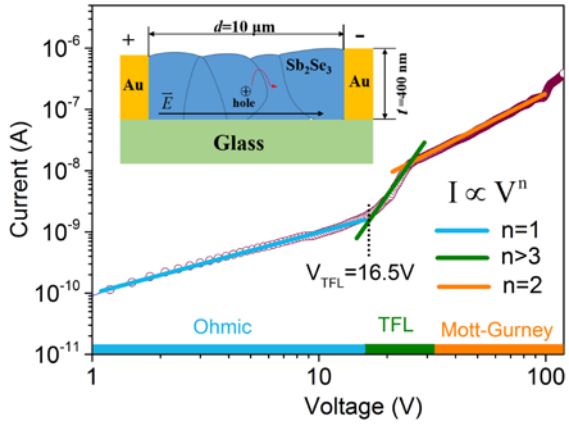

Figure S2. Mobility measurements of Sb_2Se_3 film. The bilogarithmic *I-V* curves. The inset is the device configuration for SCLC measurement.

3. Theory and experiment of Hall measurement

The formula of Hall coefficient is shown as Equation (S2).[2]

$$R_H = \frac{1}{q}\frac{p\mu_h^2 - n\mu_e^2}{\left(p\mu_h + n\mu_e\right)^2} \tag{S2}$$

To replace μ_e/μ_h with b for simplification, the Hall coefficient is simplified to Equation (S3).

$$R_H == \frac{1}{q}\frac{p - nb^2}{\left(p + nb\right)^2} \tag{S3}$$

If the intrinsic excitation is dominant at high temperature, $n_i=n=p$, the Hall coefficient can be simplified to Equation (S4).

$$R_H == \frac{1}{qn_i}\frac{1-b}{1+b} \tag{S4}$$

The relation of conductivity and mobility is as to Equation (S5).

$$\sigma = n_i q(\mu_e + \mu_h) \tag{S5}$$

The Hall mobility can be written as Equation (S6).

$$\mu = \left|R_H\sigma\right| = \left|\mu_h - \mu_e\right| \tag{S6}$$

In addition, the carrier concentration is written as Equation (S7).

$$n = p = \frac{1}{qR_H} = n_i\frac{1+b}{1-b} \tag{S7}$$

Under the intrinsic excitation, if the electron mobility is larger than that of hole, the Hall coefficient will be negative.

Hall effect measurement was conducted on Ecopia HMS-5500 using the device structure Sb_2Se_3/glass with the size of 3 mm×3 mm× 400 nm in dark. All four electrodes are Au. The

applied magnetic field intensity was 0.56 T. The temperature was controlled by resistance wire. Before test, we waited for 15 min to insure the stationary temperature.

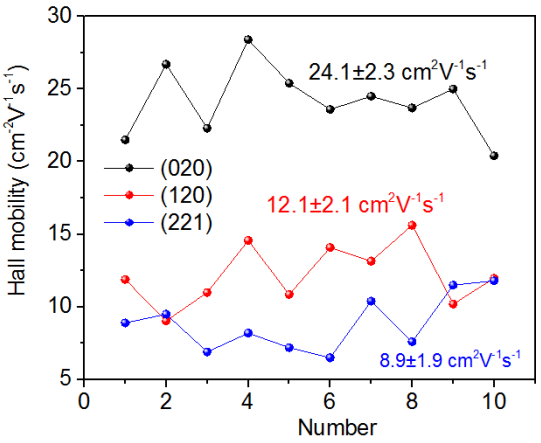

Figure S3. Hall mobility $|\mu_e$-$\mu_h|$ of 24.1±2.3, 12.1±2.1 and 8.9±1.9 cm^{2}V^{-1}s^{-1} were measured at 380 K for (020)-, (120)- and (221)-Sb_2Se_3 films.

[1] R. H. Bube, J. Appl. Phys. **1962**, 33, 1733.

[2] R. A. Smith, *Semiconductors*, Cambridge University Press, Cambridge, CB2 8BS, United Kingdom **1959**.